Fe/Rh (100) multilayer magnetism probed by x-ray magnetic circular dichroism

M. A. Tomaz, D. C. Ingram, and G. R. Harp
Department of Physics and Astronomy, Ohio University, Athens, Ohio 45701

D. Lederman and E. Mayo
Department of Physics, West Virginia University, Morgantown, West Virginia 26506-6315

W. L. O'Brien
Synchrotron Radiation Center, University of Wisconsin-Madison, 3731 Schneider Drive, Stoughton, Wisconsin 53589
(Received 10 April 1997)

We report the layer-averaged magnetic moments of both Fe and Rh in sputtered Fe/Rh (100) multilayer thin films as measured by x-ray magnetic circular dichroism. We observe two distinct regimes in these films. The first is characterized by Rh moments of at least $1\mu_B$, Fe moments enhanced as much as 30% above bulk, and a bct crystal structure. The second regime is distinguished by sharp declines of both Fe and Rh moments accompanied by a transition to an fct crystal lattice. The demarcation between the two regions is identified as the layer thickness for which both bct and fct phases first coexist, which we term the critical thickness t_{crit}. We attribute the change in magnetic behavior to the structural transformation.[S0163-1829(97)07433-X]

Thin-film multilayer systems are an area of intense research today partly due to the applications potential of magnetic properties such as the giant magnetoresistance.[1,2] Such systems also provide a venue for the exploration of fundamental issues in magnetism. One such issue is that of induced moments in normally paramagnetic materials in proximity to a ferromagnetic material. The late 4*d* transition metals (TM) are interesting candidates in light of their chemical similarity to the 3*d* ferromagnetic TM. In spite of this similarity, the 4*d* TM lack intrinsic magnetic moments in the bulk. There is a plethora of work addressing induced moments on 4*d* TM atoms in magnetic alloys.[3] Here we employ the thin-film multilayer geometry to place the paramagnetic material in proximity to the ferromagnet. This additionally provides for the observation of effects due to reduced dimensions and/or the existence of interfaces.

Epitaxial growth of metal films may lead to lattice strain and atomic volume variations due to lattice mismatches. These in turn may impact the system's magnetics. Moruzzi and Marcus[4] calculated that Rh and Pd exhibit an anomolous magnetic behavior with respect to the increase in atomic volume. They had previously shown that all transition metals exhibit a well defined onset to magnetic behavior at some critical volume. They found that the magnetic moments for Rh and Pd exceeded the Hund's rule atomic limit at the onset of magnetism and decreased toward this limit as the atomic volume was further increased. All other TM elements increase toward the Hund's rule magnetic moment limit as the atomic volume increases. There is also a simple rule that relates magnetism to the local atomic environment: the lower the coordination number the larger the atomic moment.[5] These two factors have been the motivation behind a body of theoretical and experimental work to determine under what conditions Rh may be magnetic. Calculations predict a ferromagnetic Rh ground state in a free-standing monolayer,[6–8] as an overlayer on MgO (001),[9] and more recently in an expanded bcc lattice.[10] Conflicting reports are found for Rh when in proximity to a noble-metal substrate. Some calculations suggest a ferromagnetic ground state for Rh on Ag and Au,[6,11] while others do not.[12,13] Experimentally, magnetism of Rh on Ag has been observed by some researchers[14] but not by others.[13,15] Also, no magnetism has been measured in Rh grown on Au.[16] Another possible method for inducing magnetic moments is to place a nonmagnetic material in proximity to a ferromagnet. In addition to the mechanisms mentioned above, the Rh moment may be further enhanced by a spin polarization due to band hybridization at the interface. We pursue this approach here.

A previous study of Rh/Fe (100) by Kachel *et al.*[17] showed that overlayers of Rh on Fe (100) are ferromagnetic at one monolayer (ML) coverage. They also found that the ferromagnetic order in the Rh overlayer persists at a coverage of 2 ML, although only the interface Rh atoms appear to be magnetic. They attributed the ferromagnetic (FM) ordering of the Rh overlayer to direct overlayer-substrate hybridization, and used a full linear augmented plane-wave calculation to predict a moment of $0.82\mu_B$ for a monolayer of Rh on an Fe(100) substrate. The above result was further investigated theoretically by Chouairi *et al.*[5] who found the polarization of the Rh overlayers, observed by Kachel *et al.*, to be more consistent with bct and fct rather than bcc or fcc configurations. Additionally, Chouairi and co-workers found an oscillatory (antiferromagnetic) behavior in the polarization of the Rh atoms in all cases they studied.

In the present work, we describe element specific magnetic moment measurements in Fe/Rh (100) multilayers using x-ray magnetic circular dichroism (XMCD).[18] Applying XMCD to 4*d* elements is a nontrivial, yet viable technique for such measurements.[19] This paper presents quantitative, element specific moment measurements of Fe/Rh (100) multilayers. We find that the Rh in these films carries a nearly constant magnetic moment as a function of t_{Rh} up to t_{crit} which varies from 3 to 5 Å depending on the Fe layer thickness. The measurements do not support the notion of an os-

cillatory polarization of the Rh in these films. Additionally, the magnetic moments in both Fe and Rh decline rapidly when t_{Rh} exceeds t_{crit}.

I. SAMPLE PREPARATION AND CHARACTERIZATION

All films used in the study were prepared by dc magnetron sputtering onto single-crystal MgO (100) oriented substrates at a sputtering pressure of 3.25 mTorr Ar in a chamber with a base pressure of 1×10^{-9} Torr. The sample holder position is centered about four sputter guns and is outfitted with a heating element. The sample holder is rotated during deposition for a more even distribution of material and also is equipped with a moveable shutter for wedge growth (no rotation during wedge growth). Rotation and shutter movements are controlled by a microcomputer interface to stepper motors, and deposition rates are monitored by crystal thickness monitors at each sputtering gun. The thickness monitors were calibrated by growing individual samples of each material and measuring their thickness by step profilometry.

One of the samples ($W1$) was characterized by Rutherford backscattering (RBS) analysis. RBS is a quantitative compositional analysis tool. The RBS data on this wedge-shaped sample are in very good agreement (better than 10%) with the assumed deposited thicknesses of both Fe and Rh. Since all samples were prepared under nearly identical conditions, the reported nominal thickness values should indeed be accurate to within 10%.

Polished MgO (100) substrates used for the wedge films described below were briefly repolished with 0.05μ alumina and H_2O, rinsed, and then introduced to the sputtering chamber via a load lock transfer mechanism. All substrates were outgassed for a minimum of one-half hour at $\geqslant$550°C prior to any material deposition. Fe base layers were subsequently deposited at 550°C on these MgO (100) substrates. The films were then allowed to cool in the ambient vacuum (approximately 4 h) prior to deposition of the multilayer. The growth temperature for the multilayers was 100°C or 200°C. The multilayer growth process is fully automated to improve consistency and reproducibility. Upon completion of the multilayer, a protective aluminum capping layer of 20 Å was deposited at less than 100°C.

The paper focuses on three sets of data derived from the following samples. The first set ($S1$) is based on a sequence of films grown using the following prescription {MgO(100)/Fe 300 Å/[Rh t_{Rh}/Fe 5 Å]$_{12}$/Al 20 Å}, where t_{Rh}=1, 2, 3, 4.5, and 6 Å (note that the $S1$ substrates were not repolished). The second set of data was obtained from a sample grown in the form of a wedge ($W1$) as follows {MgO(100)/Fe 40 Å/[Rh t_{Rh}/Fe 7.5 Å]$_{20}$/Al 20 Å}, where t_{Rh} is varied from 0 to 20 Å. The final data set was obtained from a wedge ($W2$) grown as {MgO(100)/Fe 40 Å/[Rh t_{Rh}/Fe 10 Å]$_{20}$/Al 20 Å}, where t_{Rh} is varied from 0 to 10 Å (note the multilayer deposition temperature was 100°C for $S1$ and $W1$, while for $W2$ it was 200°C).

A. Structural characterization by XRD

The films were characterized by high-angle specular x-ray diffraction (XRD) using a fixed anode diffractometer with 1° angular resolution, two circle goniometer, and Cu $K\alpha$ radiation. This yields information on the average lattice spacing along the growth direction. The XRD data indicate highly oriented films in the growth direction as shown in Fig. 1. The features are identified in moving from low to high angles as follows. The first peak at 43° corresponds to the substrate MgO (200) reflection. Note that there is a fairly broad shoulder extending to nearly 50° and that the terminus of this shoulder is punctuated by a small feature at 49.3° (see panel b). The shoulder is related to the MgO (200) peak, while the small peak at 49.3° is due to the fcc-like Fe/Rh (200) multilayer reflection (this scan is at t_{crit} for $S1$). The small sharp feature at 55°, attributed to defects in the substrate crystal, appears in all of our (100) samples regardless of film constituency. The feature at 60° is associated with the bcc-like Fe/Rh (200) multilayer reflection and appears to have a small shoulder associated with it in the $S1$ films which is not present in the $W1$ or $W2$ films. The difference in the $S1$ and $W1$ or $W2$ films is the thickness of the base layer; 300 Å for $S1$ vs 40 Å for $W1$ and $W2$. The feature at 65.2° is the Fe (200) reflection due to the thick base layer. The final feature at 94° is the substrate MgO (400) reflection. Panel c shows the rocking curve taken at the bcc-like Fe/Rh (200) multilayer peak of 60° which possesses a full width at half maximum (FWHM) of 0.93°.

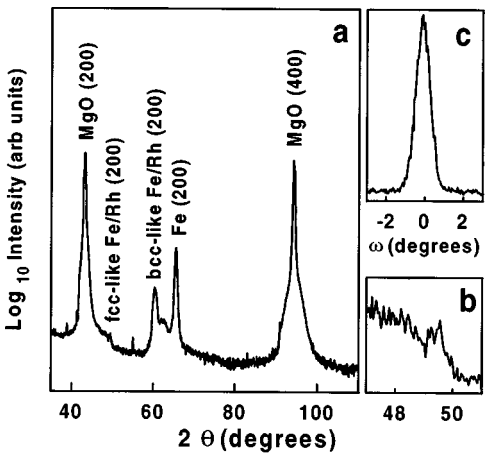

FIG. 1. (a) The XRD θ–2θ scan for the $S1$ sample with t_{Rh}=3 Å. The MgO substrate, Fe/Rh multilayer, and Fe base layer features are identified. (b) An enlarged view of the fcc-like Fe/Rh multilayer feature. (c) The rocking curve of the bcc-like Fe/Rh (200) reflection which has a FWHM of 0.93°.

The XRD data suggest that a structural phase transition occurs in these films. This is demonstrated in a representative sequence of scans given as Fig. 2. The sequence tracks the evolution of the spectral feature(s) associated with the Fe/Rh (200) multilayer reflection for the film $W2$. The left-hand panels show a smooth motion of the bcc-like ML peak to larger lattice constant accompanied by some degradation of the peak in terms of intensity and sharpness by t_{Rh}=4 Å. The sequence in the right-hand panels shows the continuing degradation of the bcc-like ML peak followed by a coexistence of both bcc-like and fcc-like ML peaks at t_{Rh}=5 Å. The fcc-like ML peak then increases in intensity and sharpness while the bcc-like feature disappears.

All the films exhibited similar behavior which is summarized in Fig. 3. Here we plot the average interplanar spacing as determined by the XRD multilayer peak angle vs t_{Rh} for

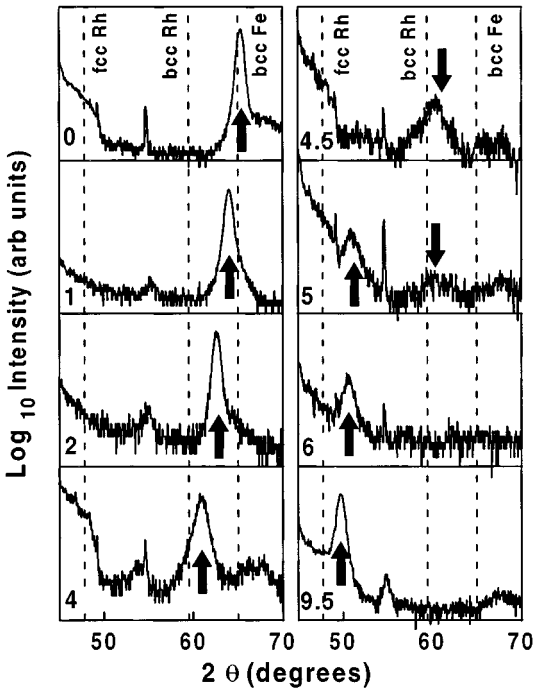

FIG. 2. A representative sequence of the θ–2θ XRD scans for $W2$ are shown. The t_{Rh} (Å) is denoted by the number in the lower left-hand corner of each frame. The Fe/Rh ML features are indicated by the arrows. The first frame is taken at the pure Fe portion of the sample and the peak is shifted to higher angle due to the ~4% lattice mismatch between Fe and the MgO substrate. The evolution of the Fe/Rh ML peak proceeds smoothly in the bcc-like region from an angle near the Bragg condition for bcc Fe ($t_{\mathrm{Rh}}=1$ Å) to an angle near the Bragg condition for bcc Rh (determined by extrapolation from the $Fe_{50}Rh_{50}$ alloy) ($t_{\mathrm{Rh}}=4$ Å). The bcc-like Fe/Rh ML peak is considerably degraded at ($t_{\mathrm{Rh}}=4.5$ Å) and subsequently two Fe/Rh ML peaks, one bcc-like and one fcc-like coexist at ($t_{\mathrm{Rh}}=5$ Å). The fcc-like Fe/Rh ML peak is the only one visible at ($t_{\mathrm{Rh}}=6$ Å). This peak continues to intensify and slide toward an angle associated with fcc Rh ($t_{\mathrm{Rh}}=9.5$ Å). Note the anomolous feature at 55° which is associated with defects in the substrate as stated in the text of the paper.

each data set. Each curve is consistent with the notion of a bcc-like lattice which transforms to an fcc-like lattice. The vertical segments of these curves indicate the t_{Rh} at which both phases first coexist. It is this point which we define as t_{crit}; interestingly it occurs at nearly the same lattice spacing in each film. As previously stated, this XRD data presented above yield only the interplanar spacing along the surface normal.

Analysis of these data is further complicated by the two possible interpretations of Rh growth on a bcc Fe template. Figure 4 is a sketch of two possible Rh unit cells. One is bcc-like, adopting the in-plane lattice constant of the Fe buffer layer, which represents an in-plane contraction of 8% when compared with bcc Rh (Ref. 20) and corresponds to an interplanar spacing of 1.82 Å.[21] The other is fcc-like, adopting an in-plane lattice constant of $\sqrt{2}$ times the in-plane lattice constant of the Fe substrate, which represents an in-plane expansion of 7% in comparison with bulk fcc Rh and corresponds to an interplanar spacing of 1.67 Å.

The linear behavior of the lattice constant in the bcc region can be interpreted in two ways. One interpretation is

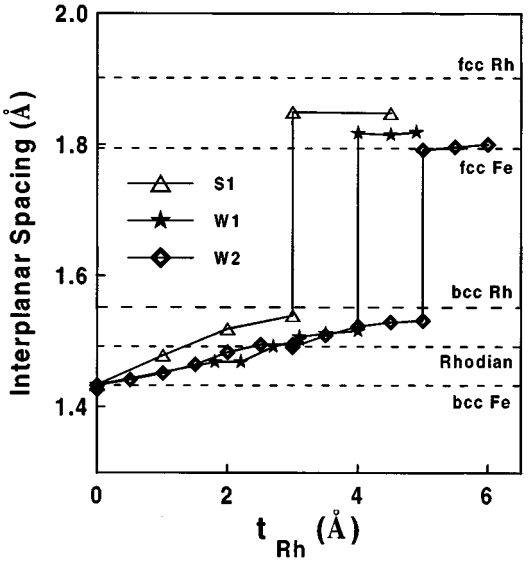

FIG. 3. The average lattice constant of the multilayer as determined from the XRD data are plotted here as a function of t_{Rh} for $S1$, $W1$, and $W2$. The vertical segment of each curve denotes t_{crit} for the particular sample. Note that the transition occurs at very nearly the same interplanar spacing in each case. The dashed lines indicate the interplanar spacings for both bcc and fcc phases of Fe and Rh. Rhodian is the name of the $Fe_{50}Rh_{50}$ alloy.

that there is extensive alloying at the interface, since the FeRh alloy lattice constant is linear in Rh concentration (at. %). The other is that the Fe and Rh layers remain essentially segregated, and the overall multilayer lattice constant is determined by an average of the Fe and Rh atomic spacings. It is known that the surface free energies of both Fe and Rh are similar, which tends to promote wetting and lead to layer-by-layer growth.[22] Two studies of Fe/Rh growth (though not of multilayers) indicate layer by layer growth, one of which claims epitaxy,[22] while the other does not.[17] These previous

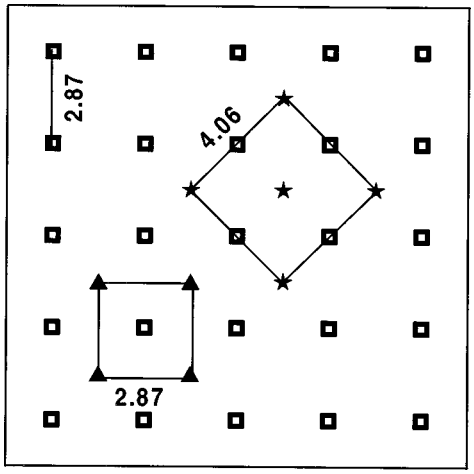

FIG. 4. A schematic of the possible interpretations of epitaxial film growth. The bcc Fe template is denoted by the open squares. The bcc Rh interpretation is denoted by the filled triangles, while the filled stars represent the fcc Rh interpretation. The in-plane lattice spacings are noted as well. The bcc Rh interpretation represents a lattice mismatch of ~+8%, while the fcc version denotes a ~−7% mismatch.

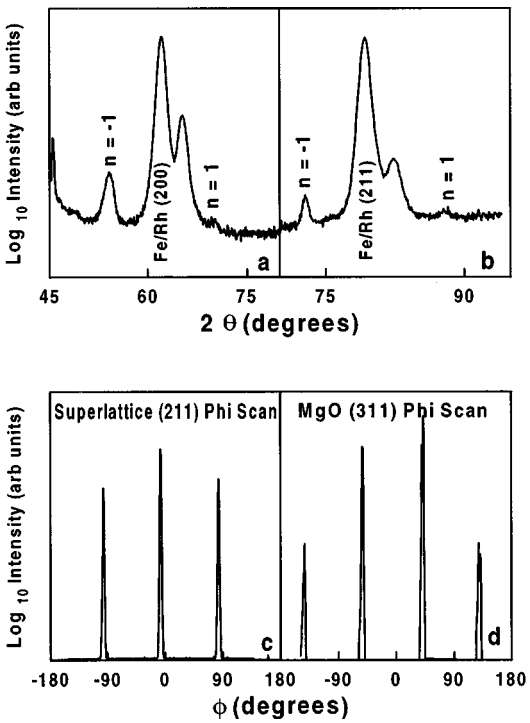

FIG. 5. XRD scans of a sample prepared as follows: {MgO(100)/Fe40 Å/[Rh 3 Å/Fe 10 Å]$_{20}$ Al 20 Å} (a) The specular $\theta-2\theta$ scan, (b) off-specular (112) $\theta-2\theta$ scan, (c) superlattice (112) ϕ scan, and (d) MgO substrate (113) ϕ scan.

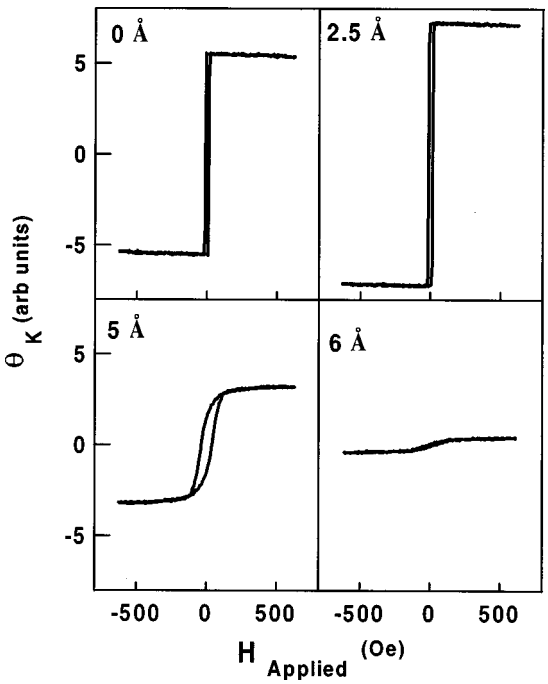

FIG. 6. A typical sequence of MOKE loops taken from *W*2. The loops show an initial increase followed by a sharp decline in the Kerr response. The decline is accompanied by an increase in the coercivity and a reduction of loop squareness. The number in the lower right-hand corner denotes t_{Rh} (Å).

results argue against an interpretation of extensive alloying between the Fe and Rh. We discuss this point further in the Appendix and find the results to be consistent with minimal alloy formation.

In order to obtain information about the film crystallography, in- and out-of-plane x-ray diffraction of a {MgO(100)/Fe40 Å/[Rh 3 Å/Fe 10 Å]$_{20}$ Al 20 Å} superlattice was performed with an 18 kW, rotating anode diffractometer equipped with a four-circle goniometer, using Cu $K\alpha$ radiation. Figure 5(a) shows the out-of-plane scan, with the momentum transfer wave vector q along the [001] direction. The main superlattice peak, corresponding to the weighted average of the Rh and Fe lattice parameters, the Fe buffer layer (002) peak, as well as the $+1$ and -1 superlattice diffraction peaks are indicated in the figure. The average out-of-plane lattice parameter of the superlattice is $a_{\mathrm{SL}}=2.99\pm0.01$ Å. The superlattice period was calculated to be $\Lambda\equiv(t_{\mathrm{Rh}}+t_{\mathrm{Fe}})=12.3$ Å from the separation between the superlattice diffraction peaks. The peak of the Fe buffer layer corresponds to a lattice parameter of $a_{\mathrm{Fe}}=2.86$ Å, in good agreement with the bulk value of 2.866 Å.

The in-plane lattice parameter was determined from Fig. 5(b), which shows an off specular scan with q along the [112] direction, indexing on a cubic unit cell. From the position of the (112) peaks, the in-plane lattice parameter of the superlattice is determined to be $a=2.91$ Å and that of the Fe buffer layer is $a=2.88$ Å. Hence, neither the superlattice nor the Fe buffer layer are perfectly cubic.

Figure 5(c) is a ϕ scan of the (112) reflection, where the sample is rotated about the [001] direction, while q remains fixed at the superlattice (112) Bragg condition. Only three peaks are visible because the [001] direction, was not perfectly normal to the surface of the film, and the outgoing beam is blocked by the sample for certain angles. No peaks were found when scanning at the (113) Bragg condition. Recall that the (113) reflection is forbidden for a bcc structure. This is strong evidence for a body-centered-tetragonal (bct) rather than a face-centered-tetragonal (fct) structure for this film.

The (113) peaks of the MgO substrate are also shown in Fig. 5(d), which determines the epitaxial relationship between the substrate and the film. Clearly, the in-plane superlattice/buffer [100] direction points along the [110] MgO direction. A similar scan of the Fe buffer layer showed that its (100) direction was oriented along the same direction as the superlattice. Hence, the superlattice is strained in-plane to match the in-plane lattice parameter of the Fe, which in turn is slightly expanded to accommodate the diagonal of the MgO unit cell (2×2.97 Å). This conclusively shows that for thin Rh layers the samples grow in a bct structure. In summary, from the above discussion we conclude that the films are epitaxial in nature, with a bct crystal structure for those samples with thin Rh layers and fct for those with thick Rh layers.

B. Magneto-optic Kerr effect magnetometry

Magneto-optical Kerr effect (MOKE) hysteresis loops were measured for all films on a Kerr magnetometer capable of achieving an 8 kOe field. The quantitative information provided by the MOKE loops includes the coercive and saturation fields (where less than 8 kOe), and the remenance percentage. The saturation Kerr rotation (θ_K^{Sat}) is also useful as an estimate of the saturation magnetization (M_{Sat}). Figure 6 shows a representative sequence of loops from *W*2 for

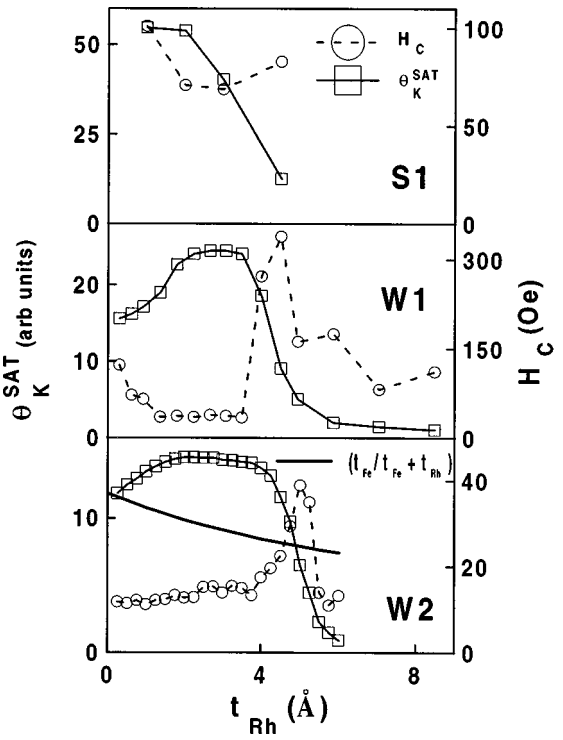

FIG. 7. The Kerr response and coercive field plotted as a function of t_{Rh} for each data set as denoted by the label in the lower left-hand corner. Note that due to the large base layer of the $S1$ samples, the cusp in coercivity is masked in comparison to the $W1$ and $W2$ data sets. Additionally, a plot of $t_{\mathrm{Fe}}/(t_{\mathrm{Rh}}+t_{\mathrm{Fe}})$ is added to the lower panel to illustrate that the magnetization behavior is not that of a simple dilution.

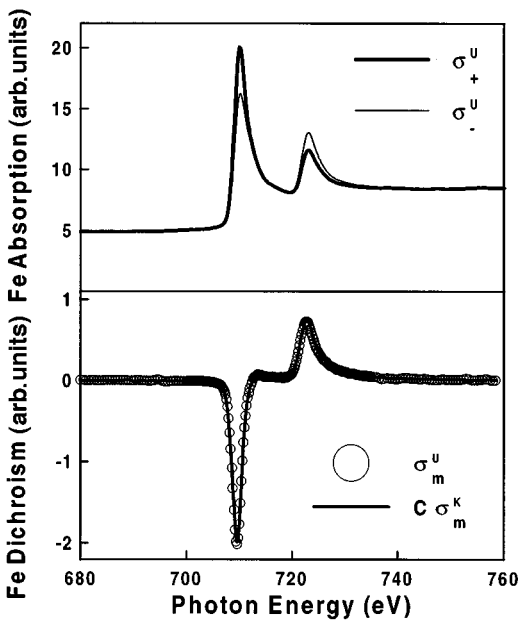

FIG. 8. The Fe absorption and dichroism spectra. The upper frame shows the σ_+^U and σ_-^U. The lower frame shows σ_m^U and $C\sigma_m^K$ where X has been minimized.

various t_{Rh}. The sequence shows an initial increase followed by a rapid decline in θ_K^{Sat}. The decline is accompanied by an increase in the coercivity and reduction of loop squareness.[23]

Figure 7 summarizes the Kerr loop data in the plots of θ_K^{Sat} and H_C as a function of t_{Rh}, which show more clearly the trend observed in the sample loops. θ_K^{Sat} initially increases, then remains level, and subsequently declines sharply. Furthermore, the decline in θ_K^{Sat} coincides with t_{crit} and the peak in H_C. Note that if Rh were nonmagnetic and the Fe moment did not change, then θ_K^{Sat} would decline approximately as $t_{\mathrm{Fe}}/(t_{\mathrm{Rh}}+t_{\mathrm{Fe}})$. The fact that θ_K^{Sat} initially increases may be due to either an enhancement of the Fe moment, the existence of an Rh moment, or both. Comparison of θ_K^{Sat} with $t_{\mathrm{Fe}}/(t_{\mathrm{Rh}}+t_{\mathrm{Fe}})$, as shown in the lower panel of Fig. 7, indicates that there is additional magnetization in these films although its source is still ambiguous.

Both $W1$ and $W2$ show a clear cusp in the coercivity, such as has been associated elsewhere with structural phase transformations.[24] This corroborates our XRD findings. H_C is also greater for $W1$ than $W2$, which can be understood from the point of view that the coercivity is derived from defects which act as pinning sites for the magnetization reversal process. Since the films undergo a structural transformation away from the equilibrium Fe structure, it is expected that the Fe layer would contain most of the defects. Thus the thinner Fe layers ($W1$) have a greater density of defects which leads to the observed increase in coercivity. The cusp in the coercivity as well as the pattern in θ_K^{Sat} are both masked in $S1$ by the 300 Å Fe buffer layer in these samples.

Finally, loops taken at different azimuthal angles yielded easy and hard magnetization axis orientations consistent with the underlying crystal. The (100) crystal planes have a fourfold symmetry, and thus four in-plane easy directions separated by 90° were observed along the ⟨010⟩ directions.

C. X-ray magnetic circular dichroism

Element specific moments were determined by analyzing XMCD spectra.[18] Briefly, XMCD is the difference in the absorption spectra for right and left circularly polarized photons. The absorption spectra are obtained by scanning the incident photon energy through a characteristic core-level edge. Element specificity is achieved as a direct result of the unique core level energies for each element.

Since the magnetic moment is mostly carried by the d electrons in the 3d FM TM, it is generally assumed that any moments induced in 4d TM will also be carried predominately by the d electrons. This means that to measure moments in 4d TM one needs to exploit p-d dipole transitions.[25] Typically, one uses the 2p edge in the 3d TM. However, the 2p levels of the 4d elements are at this time inaccessible by our instrument.[26] Thus 3p-4d transitions must be utilized for 4d XMCD which results in less intense spectral features, making 4d moment measurements a difficult task.[19] Figures 8 and 9 show the Fe and Rh absorption and dichroism spectra for $W2$ at $t_{\mathrm{Rh}}=2$ Å. These figures clearly illustrate the differences discussed above and highlight the sensitivity of the XMCD technique. In the upper panel of each figure, note that the Fe absorption feature associated with the $2p_{3/2}$ level is more than 50 times larger than that of the Rh $3p_{3/2}$. The Rh spectra are truncated at 530 eV due to the onset of the oxygen 1s edge.

X-ray absorption spectra were obtained at the Synchrotron Radiation Center in Stoughton, WI, on the 10 m TGM

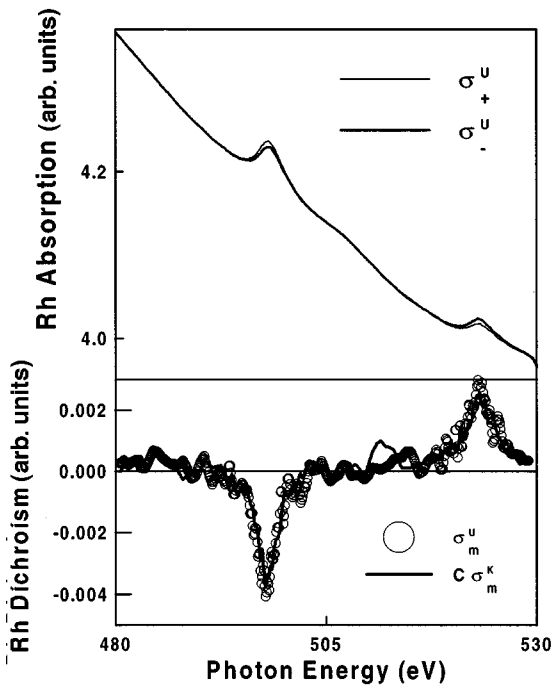

FIG. 9. The Rh absorption and dichroism spectra. The upper frame shows the σ_+^U and σ_-^U The lower frame shows σ_m^U and $C\sigma_m^K$ where X has been minimized. It is interesting to note that there is some fine structure which appears in both σ_m^U and $C\sigma_m^K$.

beamline. The beamline is equipped with a water-cooled scanning vertical aperture which allows for the selection of linear, right-hand, and left-hand elliptically polarized photons in the soft x-ray region of 200–900 eV. The degree of circular polarization when all but either the top or bottom 10% of the beam is blocked is $85\pm5\%$.[27] The samples were measured in a vacuum chamber designed specifically for XMCD, which is equipped with an electromagnet capable of producing fields of up to 1.5 kOe. The sample holder and manipulator accommodate x and y travel of $\sim$3 cm and z travel of $\sim$15 cm which provides the space to simultaneously load numerous samples. The sample holder also has a 360° rotational capability yielding a variety of geometries in which to study in- and out-of-plane moments. The sample chamber is equipped with a cylindrical collection plate which may be biased up to 2 kV for total yield measurements. The samples were introduced to the vacuum chamber with the easy axis of magnetization aligned parallel to the applied field direction and the surface normal at 45° with respect to the incident radiation beam. The sample can then be magnetized in either of two directions such that the angle between the magnetization and the incident photon beam is 45° or 135° as depicted in Fig. 10. All measurements are made in the total yield mode, which in the geometry used has been shown to be accurate to within 5%.[28]

The moment associated with a given spectrum was determined by comparing it with the spectrum of a reference sample. The reference sample we use here is a thin-film alloy of $Fe_{0.75}Rh_{0.25}$ prepared by codeposition on a Si_2O_3 substrate held at 300°C. FeRh alloys have been studied by polarized neutron reflectivity and Mossbauer spectroscopy, and the accepted values for the Fe and Rh moments of the $Fe_{0.75}Rh_{0.25}$ alloy are 2.77 and $1.0\mu_B$ respectively.[3,29] A 250

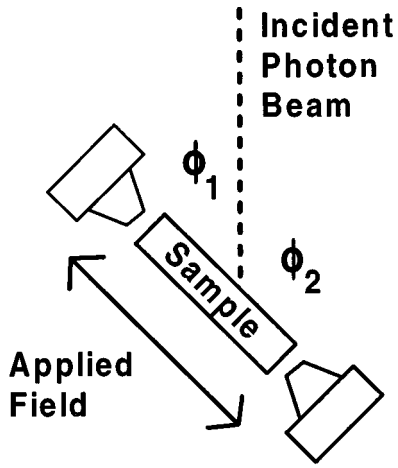

FIG. 10. The experimental configuration showing the direction of the incident photon beam and the relative orientation of the sample. The applied field can assume one of two directions resulting in either a 45° or 135° angle between the sample magnetization and incident photon wave vectors.

Å pure Fe sample was grown as well to independently calibrate the Fe signal. A comparison of the alloy XMCD with that of the pure Fe sample yielded an Fe moment of $2.84\mu_B$ in the alloy, in good agreement with previous measurements.[3,29] To arrive at this moment value, we assumed that the pure Fe sample has the bulk moment of 2.18 μ_B. To determine Rh moments, we assume that the Rh spectrum from the alloy represents a moment of $1\mu_B$. The process described above has previously been used to measure element specific moments in Fe/Cr and Fe/V multilayers via XMCD.[30,31]

In order to describe the data analysis procedure more clearly, we define the following quantities: I_S is the sample drain current (total electron yield), I_0 is the Cu mesh current (total yield used for normalization), $\sigma_+^\alpha, \sigma_-^\alpha = I_S/I_0$ for $\pm\mathbf{M}$, $\sigma_0^\alpha = \sigma_+^\alpha + \sigma_-^\alpha$, $\sigma_m^\alpha = \sigma_-^\alpha - \sigma_+^\alpha$, where σ denotes the normalized absorption spectrum and the subscripts $+$, $-$, 0, and m represent parallel, antiparallel, sum, and difference, respectively (parallel and antiparallel refer to the orientation of the projection of the incident photon wave vector on to the sample magnetization), and α represents known (K) or unknown (U).

Once reference spectra are available, the comparison proceeds as follows. First, σ_0^K and σ_0^U are set to the same scale by finding the constants A and B such that $\sigma_0^K = A + B\sigma_0^U$. Once scaled, σ_m^K and σ_m^U are formed and the quantity

$$X = \sum_{(\hbar\omega)} [C\sigma_m^K(\hbar\omega) - \sigma_m^U(\hbar\omega)]^2 \qquad (1)$$

is minimized by variation of the constant C. The moment in the unknown sample is then given by $\mu^U = C\mu^K$.

An estimate of the statistical error is the change in C (δC) which yields a 10% change in X. We use this quantity as our error bars in Fig. 12.[32] We emphasize the statistical nature of this error bar and point out that the XMCD technique has an inherent error of the order of 20%.[30,32] The lower panel of Figs. 8 and 9 show $C\sigma_m^K$ and σ_m^U for Fe and Rh, respectively, where X has been minimized.

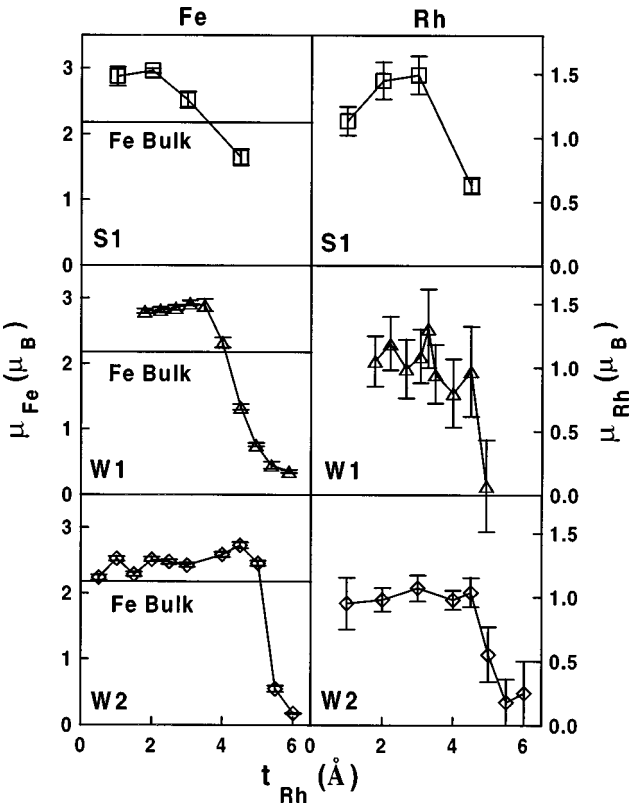

FIG. 11. The moments as determined by XMCD are shown for each set of samples. The Fe moments in the left-hand panels and the Rh moments in the right-hand panels. All are plotted vs t_{Rh}.

II. RESULTS AND DISCUSSION

The Fe and Rh moments as measured by XMCD are presented in Fig. 11. A trend which is immediately apparent is that there are two distinct regions. The first region is characterized by slightly increasing moments, and the second by a sharp decline. The demarcation between the two regions is in good agreement with t_{crit}. Thus, the films are ferromagnetic when the structure is bct and nonmagnetic when fct.

In the case of Fe, the ferromagnetic bcc structure is the equilibrium state. The Fe fcc structure is metastable and the magnetism in this phase is strongly dependent on the atomic volume.[33] Bland and co-workers[34] found that for fcc Fe epitaxially grown on Rh, no magnetic moment exists on the Fe. Calculations of tetragonally distorted Fe (Ref. 35) also show a dependence of magnetic phase on atomic volume. Here we observe that in the post-critical region, where the films are fct, the Fe loses its moment. Thus we attribute the loss of Fe moment to the structural phase transformation.

Note that the Rh and Fe moments start to decline at roughly the same value of t_{Rh}. This is an indication that the Rh magnetism is driven by the Fe layers. Interestingly, the Fe moment below this Rh thickness is greater than the Fe bulk value, and thus the presence of the Rh appears to enhance the Fe moment.

Although the layer-averaged Rh moments tend to decrease slightly beyond a t_{Rh} where it would be considered to be all interfacial ($\sim$3 Å), this decrease is much slower than would be expected from a dilution model. Thus it appears that for $t_{\mathrm{Rh}} < t_{\mathrm{crit}}$, all Rh atoms, even those in the interior of the Rh layer, possess a significant moment.

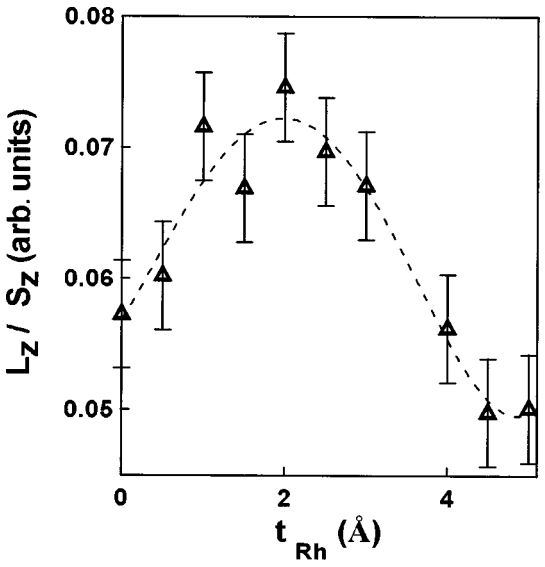

FIG. 12. The L_Z/S_Z ratio variation in the Fe moments of the $W2$ data set. The ratio is significantly enhanced in the $t_{\mathrm{Rh}}=1-3$ Å range. The error bars shown are statistical in nature and assume that there is no change in the dipole correction term. We also note here that the validity of the sum rules for noncubic systems is an open question.

The conclusion that the Rh polarization range is longer than one monolayer is further supported by the fact that the Rh moments initially *increase* in each of the sample sets with the increase being most pronounced in $S1$. Thus the Rh moment probably arises from a long-range polarization and a structural effect. This behavior is qualitatively different from the behavior of Cr or V moments in thin film multilayers with Fe.[30,31] In those cases, the Cr and V moments exhibit a strong monotonic decrease with increasing Cr or V thickness.

All samples show an enhancement of the Fe moment in the precritical region which is consistent with the notion that the mere presence of an interface can lead to a larger moment. The physical arguments for this are treated in detail elsewhere.[36] The Fe enhancement decreases with increasing Fe layer thickness. Table I shows the degree of enhancement to be inversely proportional to the Fe layer thickness and to scale exactly with the interface percentage. The interface percentage used in Table I was calculated by assuming that each interface is composed of one monolayer of Fe which is approximately 1.5 Å thick along the (100) direction. Thus, the Fe in $S1$ is 60% interfacial, and so on. Note that the enhancement scales exactly with the interface percentage regardless of the assumption made as to the amount of interfacial material.

The Rh moments show a similar, although not identical

TABLE I. Calculated percentages of interfacial Fe and enhanced moments of Fe in the precritical region. The average precritical Rh moment is given as well.

t_{Fe}	5 Å	7.5 Å	10 Å
t_{crit}	3 Å	4 Å	5 Å
$\mathrm{Fe}_{\mathrm{enh}}$ (precritical avg)	29%	19%	14%
Fe interface %	60%	40%	30%
μ_{Rh} (precritical avg)	1.36	1.10	1.00

TABLE II. Alloy formation analysis for each sample. The first column indicates the sample and Rh thickness. The second column gives the Fe moment (where applicable) followed by the third column which gives the lattice constant taken from the XRD data. Column four gives the alloy composition corresponding to the lattice constant. Column five shows the Fe thickness involved in such an alloy under the assumption that all the Rh is consumed in the alloy. The final column states the percentage of the total deposited material consumed by such an alloy.

t_{Rh} (Å)	μ_{Fe} (μ_B)	XRD L.C. (Å)	Equiv. alloy composition	t_{Fe}^{Alloy} (Å)	% Alloy
*S*1					
1.0	3.01	1.48	$Fe_{62}Rh_{38}$	1.62	0.44
2.0	2.96	1.52	$Fe_{27}Rh_{73}$	0.75	0.39
3.0	2.52	1.54 and 1.85	$Fe_{10}Rh_{90}$	0.34	0.42
4.5	2.02	1.85			
6.0		1.83			
12.0		1.86			
*W*1					
1.8	2.64	1.47	$Fe_{70}Rh_{30}$	4.20	0.64
2.2	2.66	1.47	$Fe_{70}Rh_{30}$	5.23	0.77
2.7	2.69	1.49	$Fe_{50}Rh_{50}$	2.71	0.53
3.1	2.75	1.50	$Fe_{40}Rh_{60}$	2.09	0.49
3.5	2.73	1.51	$Fe_{34}Rh_{66}$	1.76	0.48
4.0	2.19	1.52 and 1.82	$Fe_{30}Rh_{70}$	1.71	0.50
4.51	1.26	1.82			
4.94	0.72	1.82			
*W*2					
0.50	2.24	1.44	$Fe_{93}Rh_{7}$	6.46	0.66
1.0	2.52	1.45	$Fe_{84}Rh_{16}$	5.36	0.58
1.5	2.29	1.46	$Fe_{63}Rh_{27}$	4.14	0.49
2.0	2.51	1.48	$Fe_{58}Rh_{42}$	2.74	0.40
2.5	2.48	1.50	$Fe_{48}Rh_{52}$	2.27	0.38
3.0	2.43	1.49	$Fe_{50}Rh_{50}$	2.96	0.46
3.5		1.51	$Fe_{36}Rh_{64}$	1.96	0.40
4.0	2.59	1.52	$Fe_{24}Rh_{76}$	1.26	0.38
4.5	2.73	1.53	$Fe_{19}Rh_{81}$	1.06	0.38
5.0	2.46	1.53 and 1.79	$Fe_{17}Rh_{83}$	1.00	0.40
5.5	0.55	1.80			
6.0	0.18	1.80			

trend in each data set. The Rh moment starts out near $1\mu_B$ and increases to an apparent peak at $t_{Rh}\sim 3$ Å. The induced Rh moments are typically larger than the maximum moment observed in FeRh alloys ($1\mu_B$ for 35 at. % Rh).[3,29] To the best of our knowledge, these induced moments are the largest observed for any 4*d* element in a multilayer system. These moments can be compared to the Pd moments in Fe/Pd multilayers of $0.3\mu_B$ (Ref. 37) and $0.4\mu_B$.[38] This perhaps can be best interpreted in terms of a magnetic polarization effect arising at the interface. Again the largest moments are observed for the thinnest Fe layers, and since Fe has the larger moment, it effectively polarizes the Rh to a greater extent. Perhaps the fact that both Fe and Rh moments are largest for the thinnest Fe layers can be best considered as a bootstrapping effect.

Another factor which implies a significant hybridization contribution to the observed magnetic behavior is the ratio of orbital to spin moment. Powerful sum rules have been developed[39] to determine this ratio from XMCD spectra although one needs to be careful in their application. Only the Fe XMCD data on *W*2 were of the required quality to apply the sum rules, and even here we make only a relative comparison rather than extract a quantitative measure. Figure 12 shows a plot of the L_z/S_z ratio as a function of the spacer thickness. We stress that this is the L_z/S_z ratio of the Fe atoms only. However, note that Rh has a spin-orbit coupling constant ~ 2.3 times that of Fe.[40] Thus, if there were any significant hybridization of Fe and Rh orbitals, one would expect an increase in the Fe orbital moment which would manifest itself as an increase in the L_z/S_z parameter. Interestingly, Fig. 12 shows a peak in the vicinity of the t_{Rh} value where Rh has its maximum magnetic moment.

Finally, we review the trend in the Fe and Rh moment rate of declination in the post critical region. In the case of Fe, the decrease in moment becomes more precipitous with increasing Fe layer thickness. This behavior may be understood in terms of the structural transition. As the Fe thickness increases, the sample retains its ability to maintain its bct phase for thicker Rh layers. Any trend related to the rate of decline in the Rh moment is masked by the uncertainties in the *W*1 data set. Nonetheless, the Rh loses its magnetic moment similarly to the Fe in these films.

III. SUMMARY REMARKS

We have presented XMCD measurments of Fe and Rh moments in a number of sputtered Fe/Rh (100) multilayer films. The observed moments are strongly correlated with the underlying crystal structure. We present evidence which favors a model of well-defined layers with minimal mixing at the interfaces. The films undergo a bct→fct structural phase transition with increasing Rh thickness.

We have clearly demonstrated that bct Rh is magnetic when placed in proximity to Fe. Moreover the Fe moment enhancement appears to be an interface effect. The Rh moments are the largest ever induced in a 4*d* TM to date and do not exist solely in the interfacial layer region. While the observed Rh magnetism is primarily due to its proximity to Fe, the ferromagnetic state is partly stabilized by its bct structure. This study raises questions as to the role of interface strain and the exact nature of the structural transformation which will be addressed in future work.

ACKNOWLEDGMENTS

This work was supported by National Science Foundation CAREER Grant No. DMR-9623246. The Synchrotron Radiation Center is supported by NSF under Grant No. DMR-9212658.

APPENDIX: EFFECTS OF INTERFACE ALLOYING

Another possible mechanism that could enhance the Fe moment is related to interface alloying. Alloy forma-

tion could also explain the Rh moments, so it is useful to explore the question of alloy formation in these films. We first consider the possibility that all of the Rh forms an alloy with the Fe. Table II presents an analysis of the observed lattice constants in terms of the equivalent bcc FeRh alloy. The alloy composition was calculated from the lattice constant corresponding to the main superlattice XRD peak, which was then used to calculate the thickness of the equivalent Fe concentration in the alloy. Finally, we determined the fraction of the known film material accounted by the composition. The equivalent Rh concentration was calculated as $\rho_{\mathrm{Rh}}=[(a^0_{\mathrm{XRD}}-a^0_{\mathrm{bcc\,Fe}})/(a^0_{\mathrm{bcc\,Rh}}-a^0_{\mathrm{bcc\,Fe}})]$, while $t^{\mathrm{Alloy}}_{\mathrm{Fe}}=t_{\mathrm{Rh}}/\rho_{\mathrm{Rh}}-t_{\mathrm{Rh}}$. The fifth column in Table II represents the fraction of the total deposited material which is taken into account by the alloy model.

Several interesting facts result. First this model on average only accounts for 50% of the deposited material. Second, the values of $t^{\mathrm{Alloy}}_{\mathrm{Fe}}$ decrease with increasing t_{Rh}, whereas one would expect $t^{\mathrm{Alloy}}_{\mathrm{Fe}}$ to increase. But even more importantly Table II suggests that the film remains magnetic in spite of alloy concentrations in excess of 55% Rh, and moreover, these alloys are still bcc-like. Both of these results contradict the bulk FeRh binary alloy phase diagram,[41] which indicates that the bcc phase does not exist above 55% Rh, and furthermore that alloys with Rh concentrations greater than 55% are nonmagnetic at room temperature. Clearly, our data is inconsistent with a model of extensive alloy formation at the Fe/Rh interfaces. In view of this, we propose that the Fe moment enhancement is primarily due to the existence of the interfaces.

[1] M. N. Baibich, J. M. Broto, A. Fert, F. Nguyen van Dau, F. Petroff, P. Etienne, G. Creuzet, A. Friederich, and J. Chazelas, Phys. Rev. Lett. **61**, 2472 (1988).

[2] G. Binasch, P. Grünberg, F. Saurenbach, and W. Zinn, Phys. Rev. B **39**, 4828 (1989).

[3] See *3d, 4d, and 5d Elements, Alloys, and Compounds*, edited by H. P. J. Wijn, Landolt-Börnstein, New Series, Group 3, Vol. 19, Pt. A (Springer-Verlag, Berlin, 1986) for a compilation of magnetic alloy work.

[4] V. L. Moruzzi and P. M. Marcus, Phys. Rev. B **39**, 471 (1989).

[5] A. Chouairi, H. Dreyssé, H. Nait-Laziz, and C. Demangeat, Phys. Rev. B **48**, 7735 (1993).

[6] M. J. Zhu, D. M. Bylander, and L. Kleinman, Phys. Rev. B **43**, 4007 (1991).

[7] A. Mokrani, H. Dreyssé, S. Bouarab, and C. Demangeat, J. Magn. Magn. Mater. **113**, 201 (1992).

[8] P. Krüger, A. Rakotomahevitra, G. Moraitis, J. C. Parlebas, and C. Demangeat, Physica B (to be published).

[9] R. Wu and A. J. Freeman, Phys. Rev. B **51**, 5408 (1995).

[10] M. van Shilfgaarde (private communication).

[11] O. Eriksson, R. C. Albers, and A. M. Boring, Phys. Rev. Lett. **66**, 1350 (1991).

[12] Jun-Hyung Cho and Myung-Ho Kang, Phys. Rev. B **52**, 13 805 (1995).

[13] M. Weinert, S. Blügel, and P. D. Johnson, Phys. Rev. Lett. **71**, 4097 (1993).

[14] H. Li, S. C. Wu, D. Tian, Y. S. Li, J. Quinn, and F. Jona, Phys. Rev. B **44**, 1438 (1991).

[15] G. A. Mulhollan, R. L. Fink, and J. L. Erskine, Phys. Rev. B **44**, 2393 (1991).

[16] C. Liu and S. D. Bader, Phys. Rev. B **44**, 12 062 (1991).

[17] T. Kachel, W. Gudat, C. Carbone, E. Vescovo, S. Blügel, U. Alkemper, and W. Eberhardt, Phys. Rev. B **46**, 12 888 (1992).

[18] G. Schütz, W. Wagner, W. Wilhelm, P. Kienle, R. Zeller, R. Frahm, and G. Materlik, Phys. Rev. Lett. **58**, 737 (1987).

[19] G. R. Harp, S. S. P. Parkin, W. L. O'Brien, and B. P. Tonner, Phys. Rev. B **51**, 3293 (1995).

[20] The bcc Rh lattice constant of 3.10 Å is estimated by extrapolation to 100% Rh of the bcc $Fe_{50}Rh_{50}$ alloy lattice constant.

[21] The interplanar spacing is calculated by conserving the atomic volume.

[22] A. M. Begley, S. K. Kim, F. Jona, and P. M. Marcus, Phys. Rev. B **48**, 1786 (1993).

[23] We have seen no evidence for antiferromagnetic (AF) coupling between the Fe layers in any of these samples. Though the Fe/Rh multilayer geometry has shown the oscillatory exchange coupling behavior, it was demonstrated in polycrystalline films, [see S. S. P. Parkin, Phys. Rev. Lett. **67**, 3598 (1991)]. We have grown a Co/Rh multilayer wedge which does exhibit the coupling thus the absence of coupling is not derived from inadequate film preparation techniques. Instead, we believe that the bct→fct phase transformation destroys ferromagnetism in the Fe layers before the first AF coupling peak.

[24] S. D. Bader, D. Li, and Z. Q. Qiu, J. Appl. Phys. **76**, 6419 (1994).

[25] G. Schültz *et al.*, Phys. Rev. Lett. **58**, 737 (1987).

[26] Current synchrotron facilities do not in general provide the neccessary combination of circularly polarized photons on beamlines with monochromators operating in the 2.5 keV range at the required resolution.

[27] R. W. C. Hansen, W. L. O'Brien, and B. P. Tonner, Nucl. Instrum. Methods Phys. Res. A **347**, 148 (1994).

[28] W. L. O'Brien and B. P. Tonner, Phys. Rev. B **50**, 12 672 (1994).

[29] G. Shirane, R. Nathans, and C. W. Chen, Phys. Rev. **134**, A1547 (1964).

[30] M. A. Tomaz, W. J. Antel, W. L. O'Brien, and G. R. Harp, Phys. Rev. B **55**, 3716 (1997).

[31] M. A. Tomaz, W. J. Antel, W. L. O'Brien, and G. R. Harp, J. Phys. Condens. Matter **9,** L179 (1997).

[32] This method assumes that the shape of the dichroism signal is independent of sample composition and thus introduces a systematic error. Recent measurements by D. Weller and coworkers estimate the systematic error (caused mainly by the magnetic dipole correction term) at 10–20 %.

[33] W. Keune, R. Habauer, U. Gonser, J. Lauer, and D. L. Williamson, J. Appl. Phys. **48**, 2976 (1977).

[34] J. A. C. Bland, D. Pescia, and R. F. Willis, Phys. Rev. Lett. **58**, 1244 (1987), and references therein.

[35] S. S. Peng and H. J. F. Hansen, Ultramicroscopy **47**, 361 (1992).

[36] O. Hjortstam, J. Trygg, J. M. Wills, B. Johansson, and O. Eriksson, Phys. Rev. B **53**, 9204 (1996), and references therein.

[37] E. E. Fullerton, D. Stoeffler, K. Ounadjela, B. Heinrich, Z. Celinski, and J. A. C. Bland, Phys. Rev. B **51**, 6364 (1995).

[38] F. Petroff *et al.* (unpublished).
[39] P. Carra, B. T. Thole, M. Altarelli, and X. Wang, Phys. Rev. Lett. **70**, 694 (1993).
[40] A. R. Mackintosh, and O. K. Anderson, in *Electrons at The Fermi Surface*, edited by M. Springford (Cambridge University Press, Cambridge, 1980).
[41] T. Massalski, *Binary Alloy Phase Diagrams* (American Society for Metals, Metals Park, OH, 1990), Vol. 2.